Exceptional points of acoustic topological boundary states

Hao Chen,[1] Jian-Lan Xie,[1,2,*] Hua-Shan Lai,[1] Xiao-Chen Sun,[1,2] Cheng He[1,2,3,†] and
Yan-Feng Chen[1,2,3,‡]

[1]*Department of Materials Science and Engineering, National Laboratory of Solid State Microstructures,
Nanjing University, Nanjing 210093, China*

[2]*Collaborative Innovation Center of Advanced Microstructures, Nanjing University, Nanjing 210093, China*

[3]*Jiangsu Key Laboratory of Artificial Functional Materials, Nanjing University, Nanjing 210093, China*

Spectral and band topologies have different degrees of freedom, usually treated separately. Recent studies have shown that spectral topology is not only related to the topological phase transition of bulk bands but can also influence the original boundary states. However, the interplay of these two topologies remains elusive, and the rich phase transitions resulting from their combination have yet to be explored. Here, we construct a two-dimensional non-Hermitian topological acoustic model using honeycomb-lattice cavity-tube configurations with controllable in-plane hopping and out-of-plane radiation losses. The phase diagram obtained is based on the interaction between trivial and nontrivial topological bands and unbroken and broken parity-time symmetry, depending on the hopping difference and loss strength trade-off. We experimentally observe novel exceptional points of topological boundary states, indicating that the energy band attraction effect is more substantial for the boundary than for the bulk. These results enrich non-Hermitian topological physics and may lead to robust yet ultrasensitive sensing applications by taking advantage of both topological and parity-time systems.

I. INTRODUCTION

The topology of many physical systems directly matches their general behaviors and can be characterized using eigenvalues or eigenvectors, two fundamental aspects of the system's Hamiltonian [1–3]. Among them, studying the topological properties through eigenvectors is specified as band topology, whose hallmark is the presence of robust boundary states [4–6]. As a Hermitian system, since the pure real eigenvalues contain no extra topological information, band topology based on eigenvectors can fully characterize the system [3]. However, recent progress has revealed that eigenvalues may not be always real under non-Hermiticity [7,8]. Taking a parity-time (PT) symmetric system, for example, when gain and loss increase to a certain extent, the original real eigenvalues turn complex [9,10]. This change is the so-called PT-phase transition and is marked by exceptional degeneracies, which can be utilized to characterize the topology of complex eigenvalues, deemed as a kind of spectral topology [11–23].

Consequently, spectral topology could possess some unique effects that surpass the Hermitian limit such as

energy band attraction (EBA) effects [24], eigenvector coalescence [25], and the non-Hermitian skin effect [17–20]. These properties have attracted much attention and have a high potential for ultrasensitive sensing applications [11, 12], light topological funneling [19], and non-Hermitian morphing [21,26]. Thus, generalized topological classifications [27–29], manipulation of topological boundary states (TBSs) [30–33], and non-Hermiticity-induced topological phase transitions [34–37] are gradually coming to the fore. However, band topology and spectral topology are usually treated separately. Since they are defined using eigenvectors and eigenvalues, respectively, they are conveniently considered as different layers that do not interfere with each other in some scenarios. Nevertheless, recent theoretical studies have suggested that EBA effects and the following exceptional points (EPs) in the TBSs [38–40] imply the interplay of two topologies; yet, currently, there is a lack of experimental verification of this.

In this work, we manipulate a two-dimensional (2D) honeycomb lattice [38–43] associated with its band topology by adjusting the intracellular and intercellular coupling. The spectral topology is further introduced by adding imaginary mass on the onsite potential. The coupling difference and imaginary masses on two distinct sublattices span a 3D phase diagram with five different phases. Among them, the presence of EPs in the TBSs

*Contact author: xiejianlan@nju.edu.cn
†Contact author: chenghe@nju.edu.cn
‡Contact author: yfchen@nju.edu.cn

demonstrates the correlation between band topology and spectral topology. To achieve a high degree of equivalence of the tight-binding model, as well as an easy introduction and manipulation of losses, we use an acoustic cavity-tube configuration for the actual construction of the theoretical model. The length of the coupling tube corresponds to the coupling strength and holes are opened in the cavity to introduce radiation loss. Measured dispersion confirms the EBA effect and the existence of EPs in the TBSs. The above results indicate that there is an inherent connection between the two topologies, while combining them will bring additional topological phases. Such EPs in the TBSs promise to explore topologically protected ultrasensitive sensing and topological slow waves.

II. MODEL AND THEORY

As shown in Fig. 1(a), we start with a tight-binding method (TBM) of the non-Hermitian Hamiltonian of the honeycomb lattice, i.e.,

$$H(k) = \begin{pmatrix} im_a & -t_0 & 0 & -t_1 e^{ik\cdot a_1} & 0 & -t_0 \\ -t_0 & im_b & -t_0 & 0 & -t_1 e^{ik\cdot(a_1+a_2)} & 0 \\ 0 & -t_0 & im_a & -t_0 & 0 & -t_1 e^{ik\cdot a_2} \\ -t_1 e^{-ik\cdot a_1} & 0 & -t_0 & im_b & -t_0 & 0 \\ 0 & -t_1 e^{-ik\cdot(a_1+a_2)} & 0 & -t_0 & im_a & -t_0 \\ -t_0 & 0 & -t_1 e^{-ik\cdot a_2} & 0 & -t_0 & im_b \end{pmatrix}, \tag{1}$$

where a_1 and a_2 are the lattice vectors, explicitly $a_1 = a(0,1)$ and $a_2 = a\left(\sqrt{3}/2, -1/2\right)$ with a as the lattice constant; moreover, t_0 and t_1 denote the intracellular hopping and intercellular hopping, respectively. The non-Hermitian is introduced by setting imaginary masses (i.e., im_a and im_b) on different sublattices, the sign on m_a and m_b determines whether there is gain or loss.

Under the Hermitian limit ($m_a = m_b = 0$), the topological properties of the system are entirely determined by the band topology. As shown in Fig. 1(b), with the increase of hopping difference $\Delta = t_1 - t_0$, the bandgap closes and reopens, indicating an inversion of the bulk band. The quantum spin Hall (QSH) topological phase transition thus occurs, and the system turns from a trivial into a nontrivial topological phase.

For non-Hermitian systems, the closure of the bandgap can also be caused by adjusting the gain and loss. Unlike the Hermitian situation, further increasing the gain and loss fails to open the bandgap and unfolds the degeneracy points into degeneracy lines and surfaces. The appearance of the exceptional degeneracies implies a PT-phase transition. This PT-phase transition of the bulk band is shown in Fig. 1(c) with fixed intracellular ($t_0 = 0.5$) and intercellular ($t_1 = 1$) hopping parameters. Due to the complex eigenvalues, different phases need to be characterized by both real and imaginary parts of the energy bands. The PT-unbroken phase indicates that the real parts maintain a bandgap and the imaginary parts degenerate to a constant value. In contrast, the PT-broken phase indicates the degeneration of real parts while the separation of imaginary ones.

Here, in order to investigate the interplay of the PT and the transition of the topological phases, we focus on the armchair-terminated lattice with an edge bandgap in its TBS, which is caused by mirror symmetry breaking [44]. The 3D phase diagram spanned by Δ, m_a, and m_b is shown in Fig. 1(e) with TBS, EP, exceptional ring (ER), trivial, and EP&ER as five different topological phases. As demonstrated in Fig. 1(d), we start from two phases caused by a topological phase transition, i.e., trivial and TBS. When the trivial phase travels through a PT-phase transition, the bulk band degenerates and exceptional rings occur, corresponding to the ER phase. For the TBS phase, after the PT-symmetry is broken, exceptional points first appear in the topological boundary states, and the system turns into the EP phase. By further increasing the broken degree of symmetry, the bulk band would also show ERs. This time, the EPs in the boundary states still exist, and the system belongs to the EP&ER phase. If the band topology and spectral topology were independent, the phases caused by a pairwise combination may only be expected to result in four cases. However, since the EBA effect is more substantial for the boundary than for the bulk, the additional phase appears, indicating the potential interplay between two topologies. The details for different phases can be seen in Table I.

III. RESULTS

A. Realization of the interplay in the passive system

Setting $\Delta = 0.5$, we can obtain a 2D slice of the phase diagram, as shown in Fig. 2(a). Here, m_a and m_b mean adding an imaginary mass on different sublattices. This
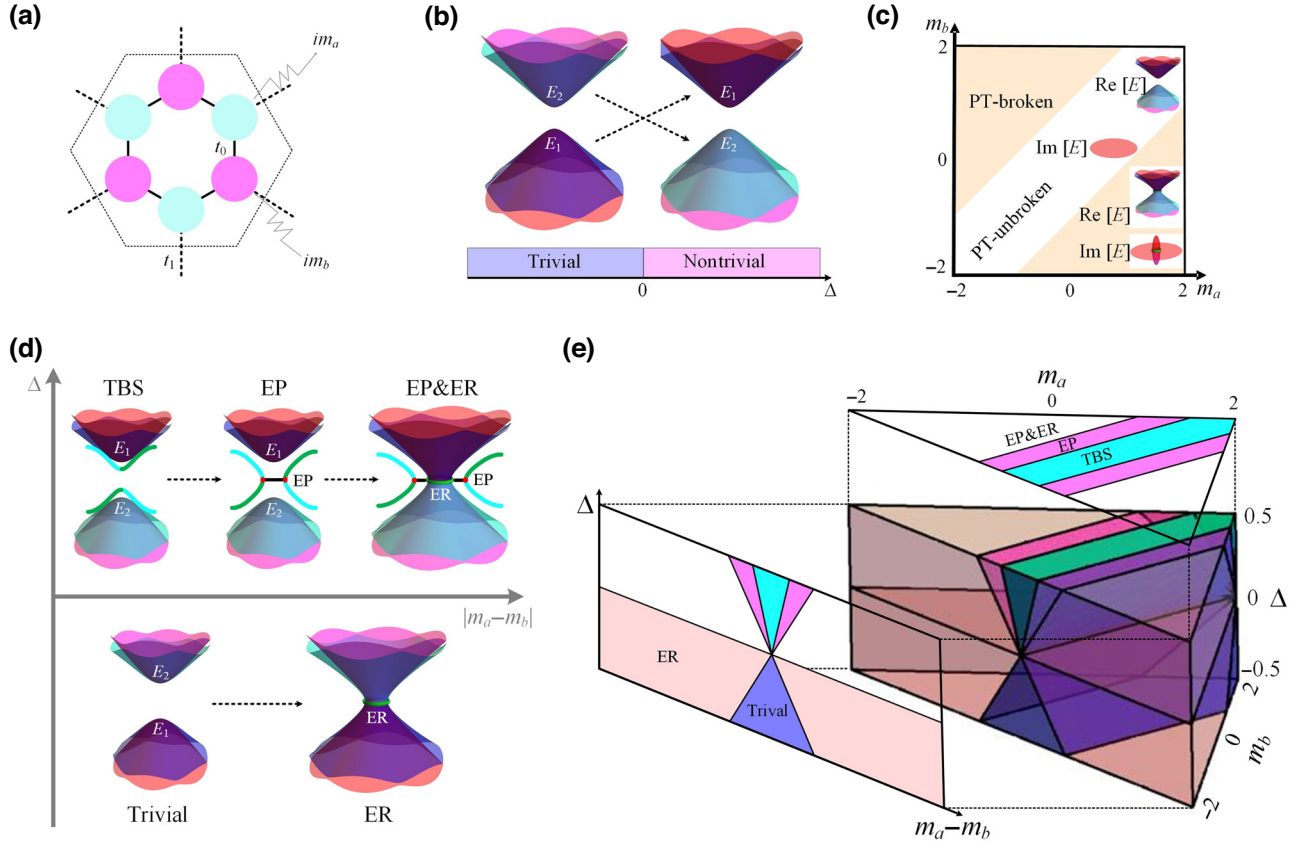
FIG. 1. (a) Phase diagrams and phase transitions for the ball-stick schematic of the non-Hermitian honeycomb lattice. (b) Phase diagrams of QSH-like topological phase transition in the Hermitian limit. (c) Phase diagrams of PT-phase transition in the bulk band. (d) Five topological phases characterized by energy band inversion and the EBA effect in the bulk and edge bands. Here, E_1 and E_2 denote two different degenerate modes, and EP and ER signify the EPs in the TBSs and the exceptional rings in the bulk band, respectively; (e) phase diagrams of the non-Hermitian topological multiple phase transitions, which are spanned by Δ, m_a, and m_b.

phase diagram divided by the spectral topology, contains the TBS, EP, and EP&ER phases, which covers the additional EP phase we are interested in.

We select the parameters on the line $m_b = 0$ and calculate the projected band of the armchair boundary, shown in Figs. 2(b)–2(d). In a Hermitian case with $m_a = 0$ [Fig. 2(b)], there is an obvious edge bandgap in the TBSs. Moreover, the imaginary part of the projected band is zero, meaning that the PT-symmetry is not spontaneously

TABLE I. Parameters of the different phases.

Hopping difference	Non-Hermitian parameters	Phases
$\Delta > 0$	$|m_a - m_b| < W_e$	TBS
	$2\Delta > |m_a - m_b| > W_e$	EP
	$|m_a - m_b| > 2\Delta$	EP&ER
$\Delta < 0$	$|m_a - m_b| < 2\Delta$	Trivial
	$|m_a - m_b| > 2\Delta$	ER

Note, $|m_a - m_b| = W_e$ and $|m_a - m_b| = 2\Delta$ are the degeneracy conditions of the edge band and bulk band, respectively, which indicate the phase transitions.
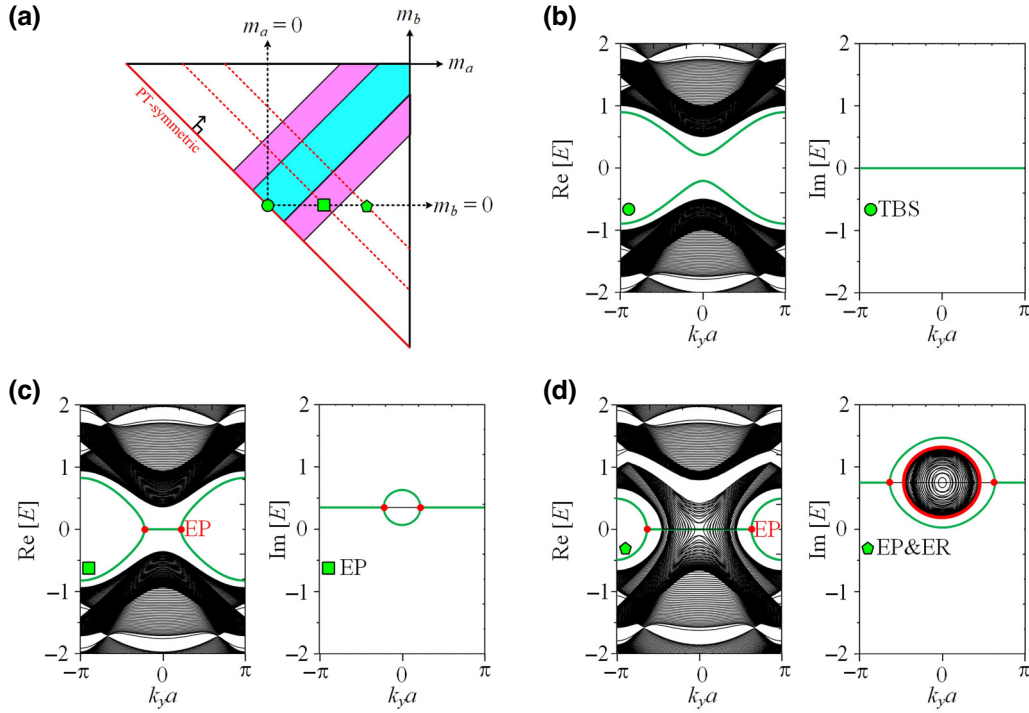
broken and the system corresponds to the TBS phase. When $m_a = 0.7$ [Fig. 2(c)], the band gap of the topological boundary states closes due to the EBA effect. The degenerate lines in the central real part match with two arcs in the imaginary part, verifying the appearance of exceptional points. The system is, thus, turned into the EP phase. However, for $m_a = 1.5$ [Fig. 2(d)], the bulk band closes because of the EBA effect and exceptional rings occur. With the coexistence of the EPs in the TBSs, the system is now in the EP&ER phase.

Usually, the spectral topology is considered under PT-symmetric conditions, corresponding to the red line $m_a + m_b = 0$ in Fig. 2(a). However, the difference is due to a constant imaginary value of the energy shift, visualized as the translation of the PT-symmetric lines. The necessity to take such parameters ($m_a > 0$, $m_b = 0$) mainly originates from experimental considerations. First, $m_b = 0$ means we only need to add gain or loss on one set of sublattices. Second, $m_a > 0$ indicates we can omit adding any gain. Since loss in acoustic systems is more convenient to realize than gain, this further reduces the difficulty in sample preparation and experiments.

FIG. 2.   Realization of the different topological phases: (a) 2D phase diagram, which is spanned by m_a and m_b. (b)–(d) Projected energy band structures for the TBS, EP, and EP&ER phases.

B. Realization of different phases in the acoustic system

Based on the non-Hermitian honeycomb lattice, our experiments utilize uniform triangular prism cavities to represent acoustic atoms; each unit cell contains six atoms, as shown in Fig. 3(a). This structure can fulfill the requirement of QSH-like topological phase transition [45]. The lattice constant a is set at 3 cm, and the height of structure h, the width of coupling tubes w, and the side length of the cavity S are $1/\sqrt{3}$, 0.13, and $0.6a/\sqrt{3}$ cm, respectively. In general, both the length and the cross-section of the coupling tube can determine the coupling strength [46]. In this work, we choose the length to control the coupling strength. The QSH-like topological phase transition is regulated by modulating l_o and l_i, corresponding to the length of intracellular and intercellular coupling tubes, respectively. Accordingly, our experiments only need to introduce loss by setting up air radiation in one set of sublattices. As shown in Fig. 3(a), purple triangular holes are opened in the triangular prism cavities to set up the air radiation. The triangular holes are scaling of the upper surface of the cavity, whose side length is $l_l = gS$. The introduced loss can be controlled by adjusting the ratio factor g, thus inducing different topological phases.

As shown in Fig. 3(b), we choose six positions in the 2D-phase diagram to demonstrate multiple topological phases. The simulations are conducted by a commercial software COMSOL based on the finite element method.

First, similar to QSH-like cases [38–43], when we set $l_o = A - 0.2a$ and $l_i = 0.8a - 2A$, bulk band inversion can be realized by modulating A. The left panels of Figs. 3(c) and 3(d) denote the band structures of trivial and non-trivial structures in the Hermitian limit with $A = a/3.25$ and $A = a/2.8$, respectively. The model becomes non-Hermitian when air radiation is introduced. Similarly, the band inversion remains unchanged and the QSH-like topological phase transition is maintained; the bulk bandgap decreases, which shows that the introduction of air radiation realizes the EBA effect in the bulk band. With the air radiation area enlarging, following the gradually increasing loss, the bulk bandgap closes and exceptional rings appear in the bulk band, as shown in the right panels of Fig. 3(c). For the trivial phase, the right panels of Fig. 3(d) show that a loss can still lead to exceptional rings. Interestingly, the closure of the bulk band usually implies the failure of the band inversion. However, this failure does not destroy the QSH-like topological phase transition, which leads to the EP and ER coexistence phenomenon.

The experimental setup is shown in Fig. 4(a). Our acoustic sample has 21×10 periods in the xy-plane with full dimensions of $63.0 \times 30 \times 1.5$ cm^3. It should be noted that, due to the mirror symmetry breaking, the obtained TBS will merge in the bulk band when there is only the nontrivial acoustic structure. This situation would result in our inability to observe the EPs in the TBSs, which can be avoided by using trivial cladding layers. Therefore, the ten
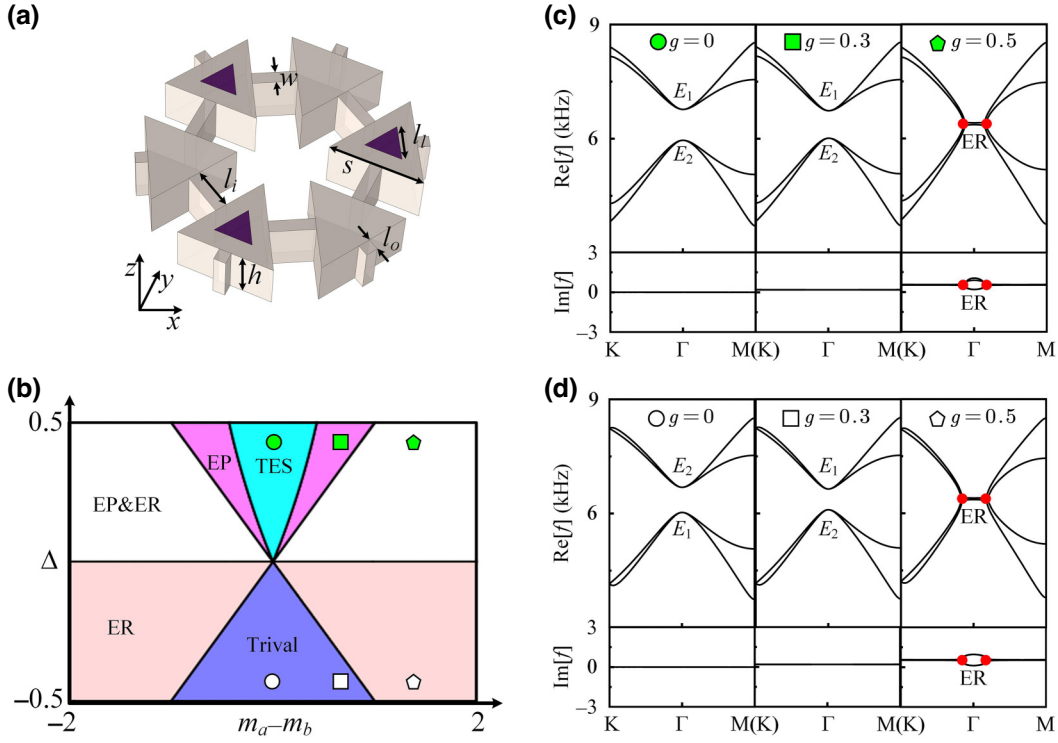
FIG. 3.　Band inversion and the EBA effect of bulk band for the non-Hermitian acoustic model: (a) non-Hermitian acoustic structure of the hexagonal unit cell; (b) phase diagrams of non-Hermitian topological multiple phase transitions, which is spanned by Δ and $(m_a - m_b)$. Numerical bulk band structures for nontrivial structures in (c) and trivial structure in (d).

periods in the x-direction consist of five nontrivial structures ($A = a/2.8$) and five trivial structures ($A = a/3.25$). The armchair-terminated edge is used in the acoustic structure, which is limited in the x-direction and is periodic in the y-direction. In our experiments, we excite the sound propagation along the interface of trivial and nontrivial structures and measure the amplitudes and phases at each site for 21 periods in the y-direction. After a Fourier transformation, we obtain the edge dispersion with a resolution of 0.1 (π/a). The measured projected bands of TBS and EP phases are shown in Figs. 4(b)–4(d).

First, we verify the existence of the topological edge states in the acoustic structure. As shown in Fig. 4(b), in the Hermitian limit ($g = 0$), due to the QSH-like topological phase transition, TBS appears in the bulk bandgap, which agrees with the theoretical prediction. There is still a mini edge bandgap between the TBSs, even in the presence of trivial cladding layers. Next, the non-Hermiticity is introduced by setting air radiation to one set of sublattices ($g = 0.2$). In the measured dispersion shown in Fig. 4(c), a flat plateau is developed near $k_y = 0$. This result corresponds to the EP phase, at which the real parts of the eigenfrequencies are degenerate and the endpoints of the plateau are EPs of the TBSs.

The acoustic energy density of the experimentally observed TBS in Fig. 4(c) is concentrated in the plateau.

The reason for this is that the introduction of loss results in the eigenvalues becoming complex and their imaginary part corresponds to the loss. In the plateau, the imaginary part of eigenfrequencies forms upper and lower edge arcs, which correspond to the largest loss and smallest loss arcs, respectively. Therefore, the acoustic energy density is concentrated on this degenerate plateau because of the smallest loss arcs [47]. We further increase the area of air radiation ($g = 0.3$), and the broadening of the plateau can be clearly seen [Fig. 4(d)], the boundary states do not reopen. These results provide an experimental validation of the interplay of a QSH-like topological phase transition and a PT-phase transition.

To further investigate the evolution of the TBSs in different topological phases, the field distributions of the TBSs with different phases at $k_y = 0.062 \, \pi/a$ were numerically calculated, as shown in Fig. 5. The simulated field distributions on the left- and right-hand side of Fig. 5 belong to the pseudospin-down and pseudospin-up TBS at $k_y = 0.062 \, \pi/a$, respectively. Here, $g = 0$, 0.2, 0.3, and 0.5 correspond to the TBS phase, the two EP phases, and the EP&ER phase, respectively. Starting from the TBS phase, the field distributions of both boundary states decrease with increasing loss. Although $g = 0.2$ and 0.3 both belong to the EP phase, the PT-phase transition occurs at $k_y = 0.062 \, \pi/a$ when $g = 0.3$. At this point, the
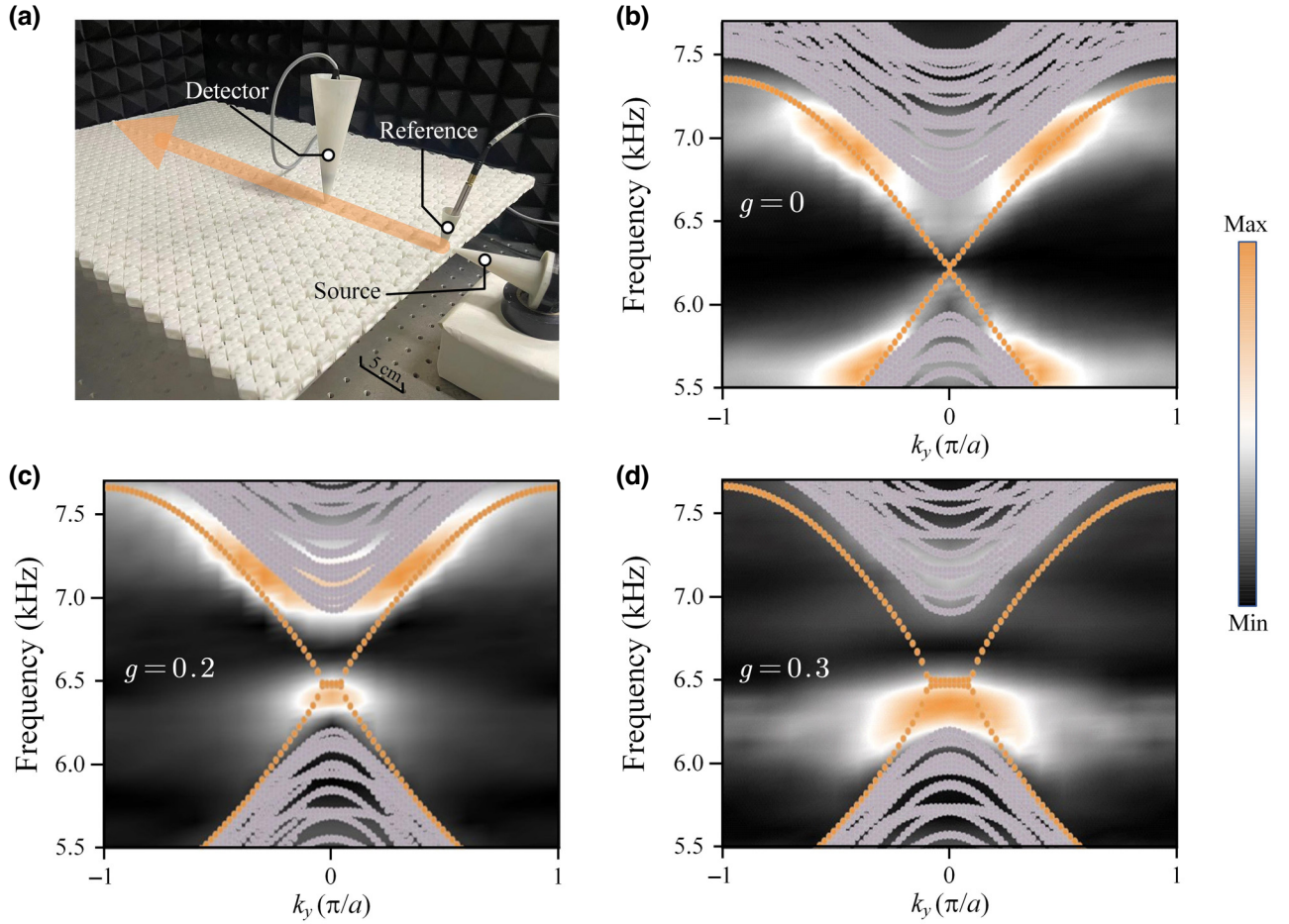
FIG. 4. Experimental observation of the TBS and EP phases: (a) experimental setup to measure the dispersion. The orange arrow marks the acoustic propagation. (b) Experimentally measured band structures for the Hermitian limit, which correspond to the TBS phase. The color bar represents the strength of the acoustic energy density with arbitrary units. The gray circles denote the calculated bulk bands. The orange circles denote the calculated topological edge band. Non-Hermitian case (c) when $g = 0.2$, which corresponds to the EP phase, and (d) when $g = 0.3$.

pseudospin-down TBS corresponds to lossy arcs with the largest loss, while the pseudospin-up TBS corresponds to gain arcs with the smallest loss. As a result, for $g = 0.3$ and 0.5, the field distribution of the pseudospin-up TBS is significantly increased, even higher than that of the Hermitian situation ($g = 0$). The above results illustrate that, while pure lossy systems inevitably exhibit energy reduction properties, the energy enhancement effect belonging to the gain system can be realized in the gain arc by constructing the passive system satisfying the PT-symmetry.

C. Topological characterizations

Our system starts from the Hermitian limit, which belongs to the realm of band topology. One commonly used approach to characterize band topology is the Wilson loop method. Choosing valence bands and a closed path $\mathcal{L}$ in momentum space, the corresponding Wilson loop can

be expressed as

$$\hat{\mathcal{W}}_{\mathcal{L}} = \hat{P}(k_1)\hat{P}(k_N)\cdots\hat{P}(k_2)\hat{P}(k_1), \tag{2}$$

where $\hat{P}(k_i) = \sum_{n \in val} |u_n(k_i)\rangle \langle u_n(k_i)|$ are valence band projectors, and k_i divide $\mathcal{L}$ into small segments. When choosing an infinite small path enclosing k, the eigenvalues of the corresponding Wilson loop matrix can be regarded as the Berry curvatures over k. The separation of the Berry curvatures can be utilized to decompose valence band space into pseudospin and pseudospinless parts [48]. The band topology can then be connected to the winding in the spectrum of separately calculated Wilson loops made on a series of paths that sweep the whole Brillouin zone. As shown in Figs. 6(a) and 6(c), the winding of pseudospin-up and pseudospin-down are -1 and $+1$ for the TBS phase, respectively, while both are 0 for the trivial phase, confirming their distinction. Compared with Figs. 6(b) and 6(d), it can be seen that introducing loss that does not
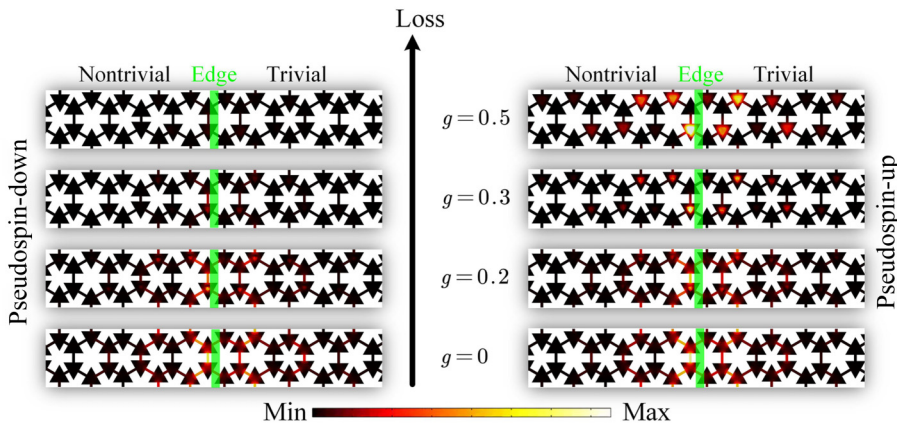
FIG. 5. Simulated evolution of the field distributions of the TBSs in different topological phases when $k_y = 0.062\,\pi/a$, the edge is marked by the green line. The trivial and nontrivial structures are marked at the top, and the color bar represents the acoustic intensity.

close the band gap will not affect the band topology. However, the appearance of EPs in TBSs cannot be inferred from the Wilson spectrum, which yields spectral topology characterizations.

The characteristic polynomial of the Hamiltonian $f(E, \boldsymbol{k}) = \det[E - H(\boldsymbol{k})]$ determines all the eigenvalues and, therefore, can be used for spectral topology characterizations [15,16]. The exceptional degeneracies in the Brillouin zone can be identified by solving the discriminant of $f(E, \boldsymbol{k})$, which is defined as

$$\Delta(\boldsymbol{k}) = \prod_{i<j} [E_i(\boldsymbol{k}) - E_j(\boldsymbol{k})]^2, \tag{3}$$
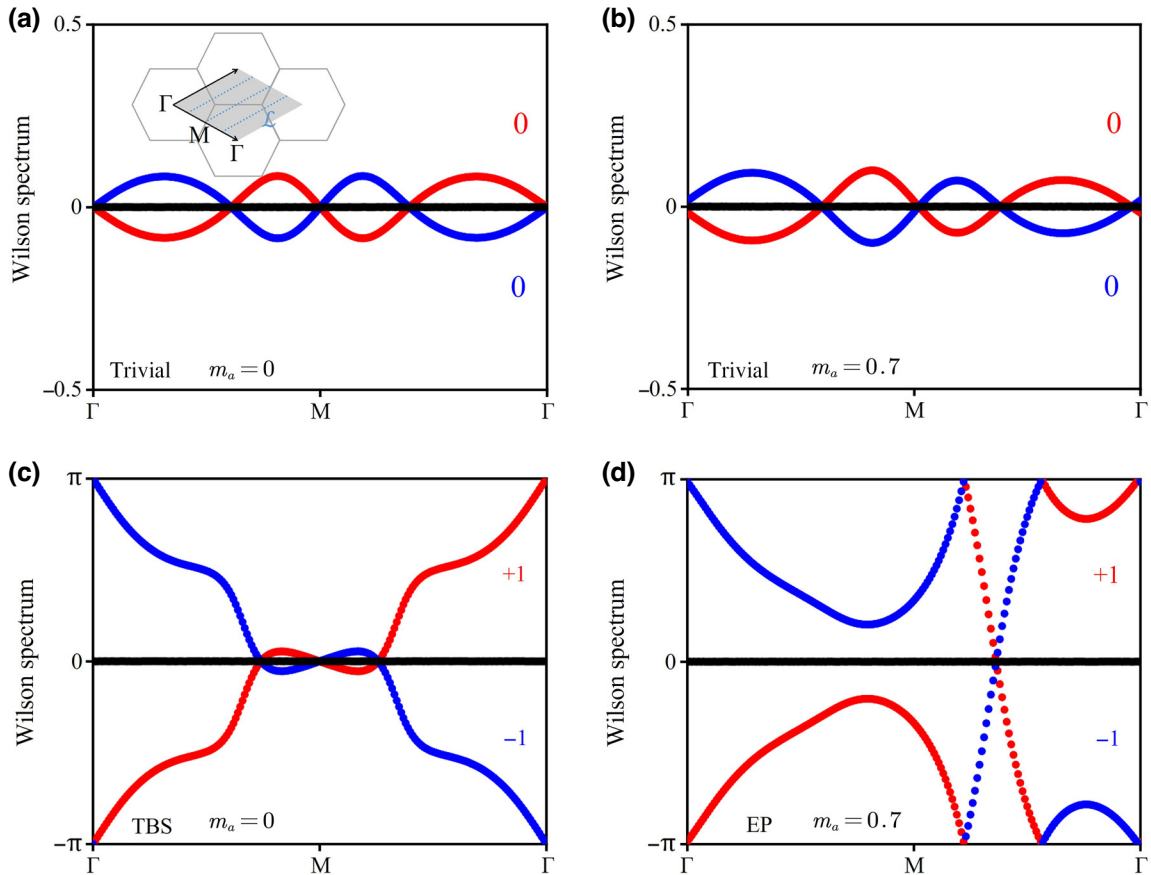

FIG. 6. Wilson spectrum of different topological phases: (a) trivial phase with $m_a = 0$, (b) trivial phase with $m_a = 0.7$, (c) TBS phase with $m_a = 0$, and (d) EP phase with $m_a = 0.7$. The valence band space can be decomposed into a pseudospin-up, pseudospin-down, and pseudospinless (i.e., three parts). Their separate windings are marked by red, blue, and black, respectively. The inset in (a) shows the series of loops used in the calculation.

where $E_i(\boldsymbol{k})$ and $E_j(\boldsymbol{k})$ represent the eigenenergy of the *i*th and *j*th band at $\boldsymbol{k}$ point, respectively.

For a non-Hermitian system, the discriminant is often a complex function of $\boldsymbol{k}$, which can be written in the form of $\Delta(\boldsymbol{k}) = \Delta_R + i\Delta_I$. Based on this property, a vector field can be defined as

$$\boldsymbol{D}(\boldsymbol{k}) = (\Delta_R, \Delta_I). \qquad (4)$$

As shown in Figs. 7(a) and 7(c), the vorticity of this vector field suggests the existence of EPs. The exact mathematical form is given as

$$v_{k^{EP}} = \frac{i}{2\pi} \oint_{C(k^{EP})} dk \cdot \nabla_k \ln \Delta(k), \qquad (5)$$

where the integration path $C(k^{EP})$ denotes a loop encircling the point k^{EP}. For the 1D situation, the calculations can be simplified. Namely, the integration path can be reduced to two positions on each side of the point. The vector field remains in terms of two directions only, as shown in Fig. 7(b). The 1D equation is

$$v_{1Dk^{EP}} = \mathrm{sgn}(\mathrm{sgn}(\Delta_{k^{EP}-C}) - \mathrm{sgn}(\Delta_{k^{EP}+C})), \qquad (6)$$

where C is a small constant, that is, $\Delta_{k^{EP}-C}$ and $\Delta_{k^{EP}+C}$ represent the discriminant of the left- and right-hand side of this point.

According to this definition, if the signs of the discriminant on both sides of the EP are opposite or the same, the topological charge of the EP is $v_{1D} = \pm 1$ or $v_{1D} = 0$, corresponding to a nontrivial or trivial EP, respectively. The topological properties of different EPs in the TBSs can then be determined using Eq. (6), and the result is shown in Fig. 7(d).

IV. DISCUSSION AND CONCLUSION

In general, drilling holes in the acoustic cavity-tube configuration not only introduces losses but also leads to a frequency shift, which can be suppressed by introducing additional sponge or putty in the holes [25,49]. Such a frequency shift can also be seen in our results when comparing Fig. 4(b) with Figs. 4(c) and 4(d). In addition, there is another frequency shift in our results, as the drilling of holes in the simulation is equated to the radiation boundaries. This is not exactly the same as those in the experiment, so the experimental measurements are slightly shifted compared with the simulation results, as shown in Figs. 4(c) and 4(d). Here, we did not introduce sponge or putty to suppress the frequency shift for the following reasons. First, due to the robustness of the topology, the EPs in the TBSs can still be realized. Second, this frequency shift is applied equally to the boundary and bulk states and, thus, a significant plateau can still be observed in experiments.
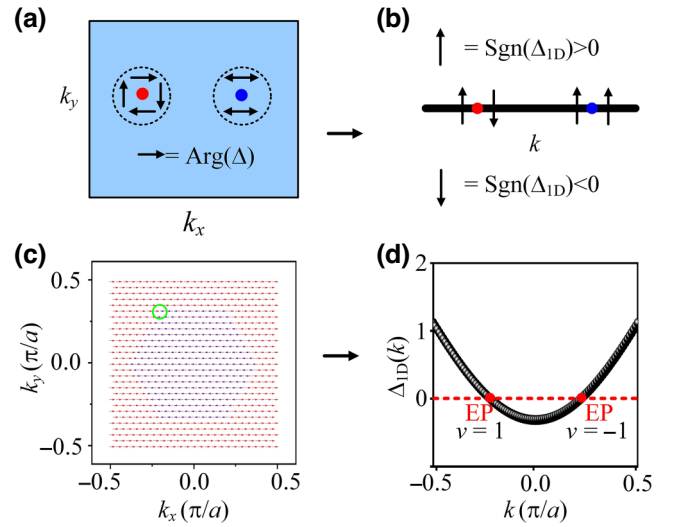

FIG. 7. Definition of the topological charge of EPs in *k*-spaces of different dimensions: (a) 2D and (b) 1D. Here, the black arrows represent the vector field distribution, and the red and blue dots represent EPs with different topologies whose topological charges are $v = 1$ and 0, respectively. (c) Distribution of the discriminant vector field of the bulk band of the TBM in 2D *k*-space, the EP is characterized by the location where the direction of the arrow changes, which is marked by the green circle. (b) Distribution of the discriminant vector field of the projected band of the TBM in 1D *k*-space. The data for the bulk band and projected band are sourced from Figs. 2(d) and 2(c), respectively.

To maintain the simplicity of our model, we do not add extra sponge or putty.

In summary, we investigate 3D phase diagrams by introducing a loss in the 2D honeycomb lattice, in which multiple phases are obtained through the interplay of PT and QSH-like phase transitions. Among them, the unique EP phase marked by the exceptional points in the TBSs is verified by acoustic experiments. Due to the EBA effect, the flat band in this EP phase can be conveniently controlled by the air radiation area, showing potential for the application of topological slow waves. Moreover, the adjustable EPs in the TBSs provide a new dimension for topological ultrasensitive sensing. The square-root dispersion near the EP causes the eigenfrequency to be extremely sensitive to changes in gas density or sound velocity [11,12] and the drilling of holes facilitates the entering of gas. As a result, the acoustic cavity-tube configuration with drilled holes provides a convenient platform for ultrasensitive gas sensing and detection. Moreover, for flat bands with gain arcs, they can be used for highly efficient slow-wave transmission in macrosonic applications [50]. These results are not limited to acoustic systems but are also suitable for other classical wave systems. In addition, our results demonstrate that the acoustic cavity-tube configuration with a drilled hole has a high potential in the field of non-Hermitian topology, which may

provide a convenient platform for more abundant non-Hermitian topological effects such as geometrically dependent non-Hermitian skin effects [51–55] and topological complex-energy braiding [56,57].

[1] D. J. Thouless, M. Kohmoto, M. P. Nightingale, and M. den Nijs, Quantized Hall conductance in a two-dimensional periodic potential, Phys. Rev. Lett. **49,** 405 (1982).

[2] W. D. Heiss, The physics of exceptional points, J. Phys. A: Math. Theor. **45,** 444016 (2012).

[3] K. Ding, C. Fang, and G. Ma, Non-Hermitian topology and exceptional-point geometries, Nat. Rev. Phys. **4,** 745 (2022).

[4] M. Z. Hasan and C. L. Kane, Colloquium: topological insulators, Rev. Mod. Phys. **82,** 3045 (2010).

[5] Z. G. Chen and Y. Wu, Tunable topological phononic crystals, Phys. Rev. Appl. **5,** 054021 (2016).

[6] S. Yves, R. Fleury, F. Lemoult, M. Fink, and G. Lerosey, Topological acoustic polaritons: robust sound manipulation at the subwavelength scale, New J. Phys. **19,** 075003 (2017).

[7] F. G. Scholtz, H. B. Geyer, and F. J. W. Nahne, Quasi-Hermitian operators in quantum mechanics and the variational principle, Ann. Phys. **213,** 74 (1992).

[8] A. Mostafazadeh, Pseudo-Hermiticity versus PT symmetry: the necessary condition for the reality of the spectrum of a non-Hermitian Hamiltonian, J. Math. Phys. **43,** 205 (2002).

[9] C. M. Bender and S. Boettcher, Real spectra in non-Hermitian Hamiltonians having PT symmetry, Phys. Rev. Lett. **80,** 5243 (1998).

[10] C. M. Bender, Making sense of non-Hermitian Hamiltonians, Rep. Prog. Phys. **70,** 947 (2007).

[11] W. Chen, ŞK Özdemir, G. Zhao, J. Wiersig, and L. Yang, Exceptional points enhance sensing in an optical microcavity, Nature (London) **548,** 192 (2017).

[12] H. Hodaei, A. U. Hassan, S. Wittek, H. Garcia-Gracia, R. El-Ganainy, D. N. Christodoulides, and M. Khajavikhan, Enhanced sensitivity at higher-order exceptional points, Nature (London) **548,** 187 (2017).

[13] M.-A. Miri and A. Alù, Exceptional points in optics and photonics, Science **363,** 6422 (2019).

[14] ŞK Özdemir, S. Rotter, F. Nori, and L. Yang, Parity–time symmetry and exceptional points in photonics, Nat. Mater. **18,** 783 (2019).

[15] Y.-X. Xiao, K. Ding, R.-Y. Zhang, Z. H. Hang, and C. T. Chan, Exceptional points make an asteroid in non-Hermitian Lieb lattice: Evolution and topological protection, Phys. Rev. B **102,** 245144 (2020).

[16] Z. Yang, A. P. Schnyder, J. Hu, and C.-K. Chiu, Fermion doubling theorems in two-dimensional non-Hermitian systems for Fermi points and exceptional points, Phys. Rev. Lett. **126,** 086401 (2021).

[17] S. Yao and Z. Wang, Edge states and topological invariants of non-Hermitian systems, Phys. Rev. Lett. **121,** 086803 (2018).

[18] N. Okuma, K. Kawabata, K. Shiozaki, and M. Sato, Topological origin of non-Hermitian skin effects, Phys. Rev. Lett. **124,** 086801 (2020).

[19] S. Weidemann, M. Kremer, T. Helbig, T. Hofmann, A. Stegmaier, M. Greiter, R. Thomale, and A. Szameit, Topological funneling of light, Science **368,** 311 (2020).

[20] X. Zhang, Y. Tian, J.-H. Jiang, M.-H. Lu, and Y.-F. Chen, Observation of higher-order non-Hermitian skin effect, Nat. Commun. **12,** 5377 (2021).

[21] W. Wang, X. Wang, and G. Ma, Non-Hermitian morphing of topological modes, Nature **608,** 50 (2022).

[22] E. J. Bergholtz, J. C. Budich, and F. K. Kunst, Exceptional topology of non-Hermitian systems, Rev. Mod. Phys. **93,** 015005 (2021).

[23] A. Li, H. Wei, M. Cotrufo, W. Chen, S. Mann, X. Ni, B. Xu, J. Chen, J. Wang, S. Fan, C.-W. Qiu, A. Alù, and L. Chen, Exceptional points and non-Hermitian photonics at the nanoscale, Nat. Nanotech. **18,** 706 (2023).

[24] M. Wu, R. Peng, J. Liu, Q. Zhao, and J. Zhou, Energy band attraction effect in non-Hermitian systems, Phys. Rev. Lett. **125,** 137703 (2020).

[25] K. Ding, G. Ma, M. Xiao, Z. Q. Zhang, and C. T. Chan, Emergence, coalescence, and topological properties of multiple exceptional points and their experimental realization, Phys. Rev. X **6,** 021007 (2016).

[26] W. Wang, X. Wang, and G. Ma, Extended state in a localized continuum, Phys. Rev. Lett. **129,** 264301 (2022).

[27] Z. Gong, Y. Ashida, K. Kawabata, K. Takasan, S. Higashikawa, and M. Ueda, Topological phases of non-Hermitian systems, Phys. Rev. X **8,** 031079 (2018).

[28] K. Kawabata, K. Shiozaki, M. Ueda, and M. Sato, Symmetry and topology in non-Hermitian physics, Phys. Rev. X **9,** 041015 (2019).

[29] H. Zhou and J. Y. Lee, Periodic table for topological bands with non-Hermitian symmetries, Phys. Rev. B **99,** 235112 (2019).

[30] M. Wang, L. Ye, J. Christensen, and Z. Liu, Valley physics in non-Hermitian artificial acoustic boron nitride, Phys. Rev. Lett. **120,** 246601 (2018).

[31] X. Ni, D. Smirnova, A. Poddubny, D. Leykam, Y. Chong, and A. B. Khanikaev, PT phase transitions of edge states at PT symmetric interfaces in non-Hermitian topological insulators, Phys. Rev. B **98,** 165129 (2018).

[32] B. Hu, Z. Zhang, H. Zhang, L. Zheng, W. Xiong, Z. Yue, X. Wang, J. Xu, Y. Cheng, X. Liu, and J. Christensen, Non-Hermitian topological whispering gallery, Nature **597,** 655 (2021).

[33] Z. Zhang, M. Rosendo López, Y. Cheng, X. Liu, and J. Christensen, Non-Hermitian sonic second-order topological insulator, Phys. Rev. Lett. **122,** 195501 (2019).

[34] K. Takata and M. Notomi, Photonic topological insulating phase induced solely by gain and loss, Phys. Rev. Lett. **121,** 213902 (2018).

[35] X.-W. Luo and C. Zhang, Higher-order topological corner states induced by gain and loss, Phys. Rev. Lett. **123,** 073601 (2019).

[36] H. T. Teo, H. Xue, and B. Zhang, Topological phase transition induced by gain and loss in a photonic Chern insulator, Phys. Rev. A **105,** 053510 (2022).

[37] H. Gao, H. Xue, Z. Gu, T. Liu, J. Zhu, and B. Zhang, Non-Hermitian route to higher-order topology in an acoustic crystal, Nat. Commun. **12,** 1888 (2021).

[38] J.-R. Jiang, W.-T. Chen, and R.-L. Chern, Parity-time phase transition in photonic crystals with C6v symmetry, Sci. Rep. **10,** 15726 (2020).

[39] X. Wang, Y. Li, X. Hu, R. Gu, Y. Ao, P. Jiang, and Q. Gong, Non-Hermitian high-quality-factor topological photonic crystal cavity, Phys. Rev. A **105,** 023531 (2022).

[40] Q.-Y. Xu, F. Liu, C.-Z. Chen, and D.-H. Xu, Edge states in a non-Hermitian topological crystalline insulator, Phys. Rev. B **105,** 075411 (2022).

[41] L.-H. Wu and X. Hu, Scheme for achieving a topological photonic crystal by using dielectric material, Phys. Rev. Lett. **114,** 223901 (2015).

[42] Z. Zhang, Q. Wei, Y. Cheng, T. Zhang, D. Wu, and X. J. Liu, Topological creation of acoustic pseudospin multipoles in a flow-free symmetry-broken metamaterial lattice, Phys. Rev. Lett. **118,** 084303 (2017).

[43] F. Liu, H.-Y. Deng, and K. Wakabayashi, Helical topological edge states in a quadrupole phase, Phys. Rev. Lett. **122,** 086804 (2019).

[44] S. E. Freeney, J. J. van den Broeke, A. J. J. Harsveld van der Veen, I. Swart, and C. Morais Smith, Edge-dependent topology in Kekulé lattices, Phys. Rev. Lett. **124,** 236404 (2020).

[45] X.-C. Sun, H. Chen, H.-S. Lai, C.-H. Xia, C. He, and Y.-F. Chen, Ideal acoustic quantum spin Hall phase in a multi-topology platform, Nat. Commun. **14,** 952 (2023).

[46] Z.-G. Chen, L. Wang, G. Zhang, and G. Ma, Chiral symmetry breaking of tight-binding models in coupled acoustic-cavity systems, Phys. Rev. Appl. **14,** 024023 (2020).

[47] J. J. Liu, Z. W. Li, Z.-G. Chen, W. Tang, A. Chen, B. Liang, G. Ma, and J.-C. Cheng, Experimental realization of Weyl exceptional rings in a synthetic three-dimensional non-Hermitian phononic crystal, Phys. Rev. Lett. **129,** 084301 (2022).

[48] S. J. Palmer and V. Giannini, Berry bands and pseudo-spin of topological photonic phases, Phys. Rev. Res. **3,** L022013 (2021).

[49] Q. Zhou, J. Wu, Z. Pu, J. Lu, X. Huang, W. Deng, M. Ke, and Z. Liu, Observation of geometry-dependent skin effect in non-Hermitian phononic crystals with exceptional points, Nat. Commun. **14,** 4569 (2023).

[50] A. Cicek, O. A. Kaya, M. Yilmaz, and B. Ulug, Slow sound propagation in a sonic crystal linear waveguide, J. Appl. Phys. **111,** 013522 (2012).

[51] K. Zhang, Z. Yang, and C. Fang, Universal non-Hermitian skin effect in two and higher dimensions, Nat. Commun. **13,** 2496 (2022).

[52] Z. Fang, M. Hu, L. Zhou, and K. Ding, Geometry-dependent skin effects in reciprocal photonic crystals, Nanophotonics **11,** 3447 (2022).

[53] K. Zhang, C. Fang, and Z. Yang, Dynamical degeneracy splitting and directional invisibility in non-Hermitian systems, Phys. Rev. Lett. **131,** 036402 (2023).

[54] Q. Zhou, J. Wu, Z. Pu, J. Lu, X. Huang, W. Deng, M. Ke, and Z. Y. Liu, Observation of exceptional points and skin effect correspondence in non-Hermitian phononic crystals, Nat. Commun. **14,** 4569 (2023).

[55] W. Wang, M. Hu, X. Wang, G. Ma, and K. Ding, Experimental realization of geometry-dependent skin effect in a reciprocal two-dimensional lattice, Phys. Rev. Lett. **131,** 207201 (2023).

[56] K. Wang, A. Dutt, C. C. Wojcik, and S. Fan, Topological complex-energy braiding of non-Hermitian bands, Nature **598,** 59 (2021).

[57] Q. Zhang, Y. Li, H. Sun, X. Liu, L. Zhao, X. Feng, X. Fan, and C. Qiu, Observation of acoustic non-Hermitian Bloch braids and associated topological phase transitions, Phys. Rev. Lett. **130,** 017201 (2023).